

# Subspace-Based Technique for Speckle Noise Reduction in SAR Images

Norashikin Yahya, *Member, IEEE*, Nidal S. Kamel, *Senior Member, IEEE*, and  
Aamir Saeed Malik, *Senior Member, IEEE*

**Abstract**—Image-subspace-based approach for speckle noise removal from synthetic aperture radar (SAR) images is proposed. The underlying principle is to apply homomorphic framework in order to convert multiplicative speckle noise into additive and then to decompose the vector space of the noisy image into signal and noise subspaces. Enhancement is performed by nulling the noise subspace and estimating the clean image from the remaining signal subspace. Linear estimator minimizing image distortion while maintaining the residual noise energy below some given threshold is used to estimate the clean image. Experiments are carried out using synthetically generated data set with controlled statistics and real SAR image of Selangor area in Malaysia. The performance of the proposed technique is compared with Lee and homomorphic wavelet in terms of noise variance reduction and preservation of radiometric edges. The results indicate moderate noise reduction by the proposed filter in comparison to Lee but with a significantly less blurry effect and a comparable performance in terms of noise reduction to wavelet but with less artifacts. The results also show better preservation of edges, texture, and point targets by the proposed filter than both Lee and wavelet and less required computational time.

**Index Terms**—Image denoising, principal component analysis (PCA), spatial filters, stochastic processes, synthetic aperture radar (SAR).

## I. INTRODUCTION

THE synthetic aperture radar (SAR) imaging technique is popular for remote sensing and monitoring applications because of its usability under various weather conditions and its ability to provide high-resolution imagery. A SAR image is generated by sending electromagnetic waves from a moving platform, spaceborne or airborne, toward the target surface and by coherently processing the returned backscattered signals from multiple distributed targets [1]. However, the coherent processing causes speckle effect [2] and gives SAR images its noisy appearance. Speckle presence appears as granular noise which reduces the image resolution [3] and may hamper the operation of image interpretation and analysis. Hence, noise filtering has become an essential part of SAR imagery systems. The objective of using a speckle reduction filter is to smooth homogeneous regions while preserving the useful textural in-

formation and structural features, such as edges. In subsequent paragraphs, we discuss the different types of adaptive filters that are used to reduce speckle noise in SAR images.

The commonly used adaptive spatial-domain filters for speckle reduction are Lee filter [4], Frost filter [5], Kuan filter [6], and enhanced Lee and modified Frost filters [7]. The assumptions made in implementing these filters are as follows: 1) The SAR speckle is modeled as a multiplicative noise; 2) the noise and signal are statistically independent; and 3) the sample mean and variance of a pixel are equal to its local mean and local variance computed within a window centered on the pixel of interest [4], [8]. The performance of these filters is highly dependent on the choice of size and orientation of the moving window.

The Lee and Kuan filters have similar formation but differ in signal model assumptions and derivation. They originate from simplified theoretical studies and are based on parameters related to local image coefficients of variation which measures the scene heterogeneity [9]. Both Lee and Kuan filters remove speckle noise by computing a linear combination of the center pixel intensity in a filter window with an average intensity of the window. Thus, the filters achieve a balance between averaging in homogeneous regions and a strict all-pass (identity) filter in edge contained regions. On the other hand, the Frost filter attempts to strike a balance between averaging and identity filter by forming an exponential-shaped filter kernel that can adaptively vary from an average filter to an identity filter. Similar to Lee and Kuan filters, the filter response varies locally with the coefficients of variation. This means that, at low coefficient variation, the filter is more average-like and, at high coefficient variation, the filter attempts to preserve sharp features by retaining its original pixel value. The enhanced Lee and Frost filter proposed by Lopes *et al.* [7] uses three variations of coefficient values, namely, low, intermediate, and high, to divide an image into homogeneous regions, heterogeneous regions, and isolated point target regions, respectively. The filter outputs a local mean at homogeneous regions and retains the original pixel at points of high activity. Generally speaking, the adaptive spatial-domain filters have the following deficiencies: 1) fail to maintain the mean value, particularly if the number of look of the original SAR data is small; 2) the highly reflective point targets are blurred; and 3) dark spotty pixels are not filtered [10].

In addition to the averaging and adaptive filters, there is speckle noise removal using wavelet transform [11]–[13]. As an outcome of wavelet theory, denoising in the discrete wavelet transform (DWT) domain may be stated as a thresholding

Manuscript received March 17, 2013; revised September 5, 2013 and November 27, 2013; accepted December 9, 2013. Date of publication January 20, 2014; date of current version May 23, 2014.

The authors are with the Department of Electrical and Electronic Engineering, Universiti Teknologi PETRONAS, 31750 Tronoh, Malaysia (e-mail: nidalkamel@petronas.com.my).

Color versions of one or more of the figures in this paper are available online at <http://ieeexplore.ieee.org>.

Digital Object Identifier 10.1109/TGRS.2013.2295824

of DWT coefficients of the noisy image. For the case of speckle noise, homomorphic filtering, in which the DWT of the log-transformed noisy image is either adaptively thresholded [14] or empirically shrunk in an adaptive fashion [15], has been utilized. The major drawbacks of such approach are the backscatter mean preservation in homogeneous areas, sharpness preservation, and ringing impairments [15], [16]. Furthermore, signal variations are damped by the logarithm, resulting in an unlikely “flatness” after filtering. To overcome these deficiencies, Argenti *et al.* in [17] proposed a minimum-mean-square error filtering performed in the undecimated wavelet domain by means of an adaptive rescaling of the detail coefficients and the local space-varying signal, where the noise statistics are estimated in the wavelet domain. In [18], using statistical modeling of wavelet coefficients, Ranjani *et al.* proposed a speckle suppression technique using dual-tree wavelet transform by putting into consideration the significant dependences of the wavelet coefficients across different scales. The interscale dependence of the wavelet coefficients in each subband is modeled using bivariate Cauchy probability density function (pdf).

In this paper, a subspace-based technique to reduce the speckle noise in SAR images is proposed. Fundamentally, the proposed technique is an extension of the original work of Ephraim and Van Trees [19] in speech enhancement toward 2-D signals. The underlying principle is to decompose the vector space of the noisy image into a signal-plus-noise subspace and the noise subspace. The noise removal is achieved by nulling the noise subspace and controlling the noise distribution in the signal subspace. For white noise, the subspace decomposition can theoretically be performed by applying the Karhunen-Loeve transform (KLT) to the noisy image. Linear estimator of the clean image is performed by minimizing image distortion while maintaining the residual noise energy below some given threshold. For colored noise, a prewhitening approach prior to KLT transform, or a generalized subspace for simultaneous diagonalization of the clean and noise covariance matrices, can be used.

The fundamental signal and noise model for subspace methods is additive noise uncorrelated with the signal. However, in SAR images, the noise is multiplicative in nature, so a homomorphic framework takes advantage of logarithmic transformation in order to convert multiplicative noise into additive noise. However, this nonlinear operation totally changes the statistics of SAR images and induces bias in their mean values. For the purpose of radiometric preservation, the biased mean needs to be corrected, along with antilog operation.

This paper is organized as follows. Section II describes the pdf of speckle noise in SAR images. Section III, covers the principle of subspace and how it can be extended to speckle noise removal. In specific, the first part of Section III covers the proposed subspace technique and its implementation in speckle noise filtering, the conceptual relationship between eigendecomposition and oriented energy, and the derivation of the optimal estimator using the principal subspace. The second part of Section III covers the implementation issues, namely, the estimation of noise variance, the method to determine the signal subspace dimension, and the optimum value of the Lagrange multiplier. Section IV is divided into two main sections. The first part of Section IV evaluates the performance of SDC

for varying image size and its ability to represent images. The second part of Section IV evaluates the performance of the proposed technique using simulated images and real SAR images in comparison to Lee filter and a wavelet filter [20], [21] in homomorphic framework. Finally, Section V concludes this paper.

For clarity, an attempt has been made to adhere to a standard notational convention. Lowercase boldface characters will generally refer to vectors. Uppercase characters will generally refer to matrices. Vector or matrix transposition will be denoted using  $(\cdot)^T$ , while transformations at the left and right sides are denoted as  $(\cdot)^L$  and  $(\cdot)^R$ , respectively.  $\mathbb{R}^{m \times m}$  denotes the real vector space of  $m \times m$  dimensions.

## II. STATISTICAL MODELING OF SPECKLE NOISE IN SAR IMAGES

With homogeneous targets and weakly textured areas in SAR images, the speckle noise is fully developed, and the multiplicative model is used to describe it. Since most available image denoising techniques were developed for additive white Gaussian noise (AWGN), it is necessary in case of a fully developed speckle noise to apply a logarithmic transform to the multiplicative model in order to convert it into additive. The process involves applying logarithmic transform prior to the denoising technique and then exponentially transforming the output to obtain the despeckled image. As a nonlinear operation, the logarithmic transform totally changes the statistics of SAR images, so the original speckle statistics cannot directly be used with the log-transformed images. In this section, the pdf, mean, and standard deviation values of the log-transformed speckle noise are briefly discussed. The purpose is to correct the biased mean for radiometric preservation.

Speckle in SAR images is caused by constructive and destructive interferences of coherent waves reflected by many elementary scatterers contained within the image resolution cell. Under the assumption that in each resolution cell: 1) no scatterers in domination over the others combined; 2) the number of scatterers is large and they are statistically identical and independent; and 3) the maximum range extent of the target is many wavelength across, it then follows that the vector sum of the backscattered electric field is equivalent to a 2-D random walk process with independently and identically distributed (i.i.d.) Gaussian real and imaginary components [22], [23].

SAR images are usually available in two formats: *intensity* and *amplitude*. For homogeneous areas, the pdf of the magnitude of the fully developed speckle is known to have Rayleigh distribution, and the phase is uniformly distributed. On the other hand, the pdf of speckle intensity is described by a negative exponential distribution [22], [23].

In SAR images, pixels are averaged in order to reduce the grainy appearance caused by the speckle noise. In this case, the statistical distribution of the resultant speckle noise is given by gamma distribution for intensity and by the multiconvolution of the Rayleigh pdf in the case of amplitude format [16]. In the subsequent paragraphs, the pdfs, mean values, and variances for the logarithmically transformed speckle noise in intensity and amplitude format are discussed.

### A. Intensity Format

If we use  $G$  to denote the SAR image intensity for a given pixel whose backscattering coefficients are  $W$  and assume that the SAR image is an average of  $L$  looks, then  $G$  is related to  $W$  by the multiplicative model [23]

$$G = WN \quad (1)$$

where  $N \in \mathbb{R}^{m \times n}$  is the random variable speckle noise matrix following a gamma distribution with unit mean and variance,  $1/L$ . The noise pdf is given by [23]

$$P_N(N) = \frac{L^L N^{L-1} e^{-LN}}{\Gamma(L)}, \quad N \geq 0 \quad (2)$$

where  $\Gamma(\cdot)$  denotes the gamma function. Applying the logarithmic function to both sides of (1), we get

$$\log(G) = \log(W) + \log(N). \quad (3)$$

Expression (3) can be rewritten as

$$Y_l = X_l + N_l \quad (4)$$

where  $Y_l, X_l$ , and  $N_l$  are the logarithms of  $G$ ,  $W$ , and  $N$ , respectively. The mean and variance of the logarithmically transformed gamma distribution are given, respectively, by [16]

$$\bar{N}_l = \psi(0, L) - \ln(L) \quad (5)$$

$$v_{N_l}^2 = \psi(1, L) \quad (6)$$

where  $\psi(i, L)$  is the polygamma function of  $L$ -looks given by

$$\psi(i, z) = \left(\frac{d}{dz}\right)^i \psi(z) = \left(\frac{d}{dz}\right)^{i+1} \ln \Gamma(z). \quad (7)$$

When  $L$  is an integer, (6) can be further simplified to

$$\bar{N}_l = \sum_{k=1}^{L-1} \frac{1}{k} + \psi(1) - \ln(L), \quad \psi(1) = -C \quad (8)$$

where  $C$  is the Euler's constant ( $C = 0.577215$ ) [16]. Moreover, the variance can be computed from [24], [25]

$$v_{N_l}^2 = \psi(1, 1) - \sum_{k=1}^{L-1} \frac{1}{k^2}, \quad \psi(1, 1) = \frac{\pi^2}{6}. \quad (9)$$

Table I shows the mean and standard deviation of Rayleigh-fading object as a function of the number of look ( $L$ ) [24]. The calculated values in Table I can be used to adjust the bias in the mean value due to homomorphic operations. It should be stressed that the bias does not depend on the mean value of the SAR intensity, which means that the bias can be corrected systematically, provided that the number of looks is rightly estimated.

TABLE I  
MEAN AND STANDARD DEVIATION OF SPECKLE NOISE  
IN LINEAR AND LOGARITHMIC SCALES [24]

$L$	$\bar{N}_l$	$v_{N_l}$	$\bar{N}_l(\text{dB})$	$v_{N_l}(\text{dB})$
1	$\bar{N}_l$	$\bar{N}_l$	$10 \log \bar{N}_l - 2.507$	5.570
2	$\bar{N}_l$	$\bar{N}_l/\sqrt{2}$	$10 \log \bar{N}_l - 1.174$	3.488
4	$\bar{N}_l$	$\bar{N}_l/\sqrt{4}$	$10 \log \bar{N}_l - 0.565$	2.314
10	$\bar{N}_l$	$\bar{N}_l/\sqrt{10}$	$10 \log \bar{N}_l - 0.221$	1.408
20	$\bar{N}_l$	$\bar{N}_l/\sqrt{20}$	$10 \log \bar{N}_l - 0.109$	0.983

### B. Amplitude Format

If (1) is in amplitude format and  $L = 1$ , then the pdf of  $N$  obeys the Rayleigh pdf [23], and the mean and variance of its logarithmic transform are given by

$$\bar{N}_l = \frac{1}{2} \ln \left( \frac{4}{\pi} \right) + \frac{1}{2} \psi(1), \quad v_{N_l}^2 = \frac{1}{4} \psi(1, 1). \quad (10)$$

For  $L > 1$  amplitude image, different techniques are used to obtain a closed analytical form for the pdf. Among these techniques, there are histogram estimation technique and approximation method using Edgeworth expansion [16].

Because of the simplicity in biased mean adjustment of intensity format in comparison to the amplitude format, we consider it for the analytical part of this paper.

## III. SUBSPACE-BASED SPATIAL DOMAIN CONSTRAINT APPROACH (SDC)

In this section, we derive the linear optimal estimator which minimizes the image distortion while constraining the energy of residual noise. The noise is assumed to be AWGN, uncorrected with the signal. However, with SAR imagery, a colored noise due to interpixel correlation in range because of oversampling is usually developed. Thus, a whitening scheme should be used prior to the implementation of the proposed subspace technique in SAR applications. Different whitening schemes are available, among them the Cholesky factorization-based technique, which is used in this paper [26].

### A. Signal and Noise Model

Assuming that the noise signal is additive, white, and uncorrelated with the image signal, the  $m \times n$  matrix of noisy image  $Y$  is given by

$$Y = X + N \quad (11)$$

where  $N \in \mathbb{R}^{m \times n}$  is the noise matrix and  $X \in \mathbb{R}^{m \times n}$  is the clean image. Let

$$\hat{X} = HY \quad (12)$$

be a linear estimator of the clean image  $X$ , where  $H \in \mathbb{R}^{m \times m}$  is known as the model matrix. The error signal  $\epsilon$  obtained from the estimation is given by

$$\epsilon = \hat{X} - X = (H - I)X + HN = \epsilon_X + \epsilon_N \quad (13)$$



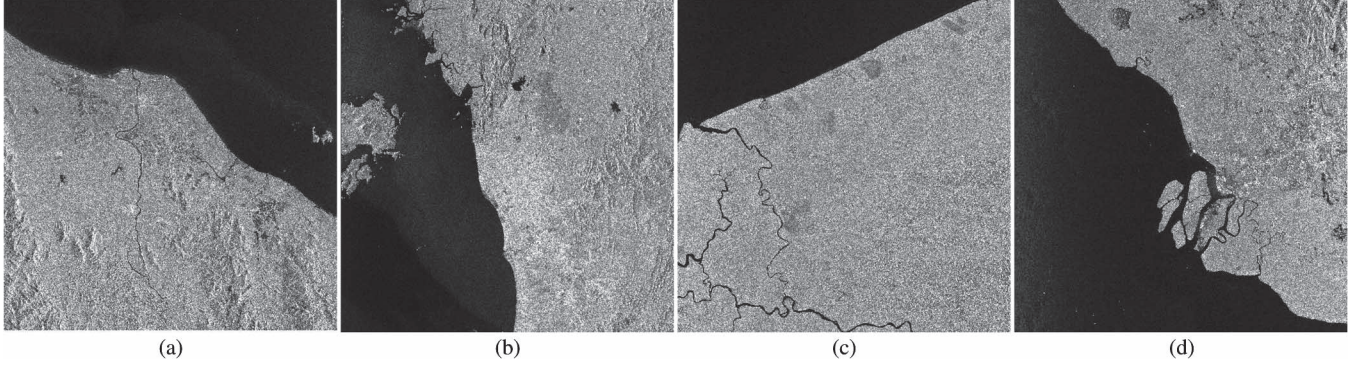


Fig. 1. Real SAR images of different terrains in Malaysia. (a) Kota Bharu. (b) Perlis. (c) Sibul. (d) Lembah Klang. *Courtesy of the Malaysian Remote Sensing Agency.*

where  $\epsilon_X$  represents image distortion and  $\epsilon_N$  represents the residual noise [19]. Defining the energies of the image distortion  $\bar{\epsilon}_X^2$  and the energies of the residual noise  $\bar{\epsilon}_N^2$  as

$$\bar{\epsilon}_X^2 = \text{tr} (E [\epsilon_X^T \epsilon_X]) \quad (14)$$

$$\bar{\epsilon}_N^2 = \text{tr} (E [\epsilon_N^T \epsilon_N]) \quad (15)$$

where  $E[\cdot]$  is the expected value, the optimum linear estimator can be obtained by solving the following spatial domain constrained optimization problem [19], [27]:

$$\min_H \bar{\epsilon}_X^2 \quad \text{subject to} \quad \frac{1}{m} \bar{\epsilon}_N^2 \leq \sigma^2 \quad (16)$$

where  $\sigma^2$  is a positive constant.

The optimum estimator is the sense of (16) that can be found using the Kuhn–Tucker necessary conditions for constrained minimization [28]. The constrained minimization described in (16) can be solved using the method of Lagrange multipliers [29]. Specifically,  $H$  is a stationary feasible point if it satisfies the gradient equation of the Lagrangian

$$\begin{aligned} L(H, \mu) &= \bar{\epsilon}_X^2 + \mu (\bar{\epsilon}_N^2 - m\sigma^2) \\ &= \text{tr} ((H - I)R_X(H - I)^T) \\ &\quad + \mu (\text{tr}(HR_NH^T) - m\sigma^2) \end{aligned} \quad (17)$$

where  $\mu \geq 0$  is the Lagrange multiplier,  $R_X$  is the covariance matrix of the clean image,  $R_N$  is the covariance matrix of the noise, and

$$\mu (\bar{\epsilon}_N^2 - m\sigma^2) = 0 \quad \text{for } \mu \geq 0. \quad (18)$$

From  $\nabla_H L(H, \mu) = 0$ , we obtain

$$\nabla_H L(H, \mu) = 2(H - I)R_X + 2\mu HR_N = 0. \quad (19)$$

Thus

$$H_{\text{SDC}} = R_X(R_X + \mu R_N)^{-1}. \quad (20)$$

In the case of white noise  $R_N = v_n^2 I$ , where  $v_n^2$  is the noise variance and  $I$  is the identity matrix, the solution for the optimum estimator  $H_{\text{SDC}}$  is given as

$$H_{\text{SDC}} = R_X (R_X + \mu v_n^2 I)^{-1}. \quad (21)$$

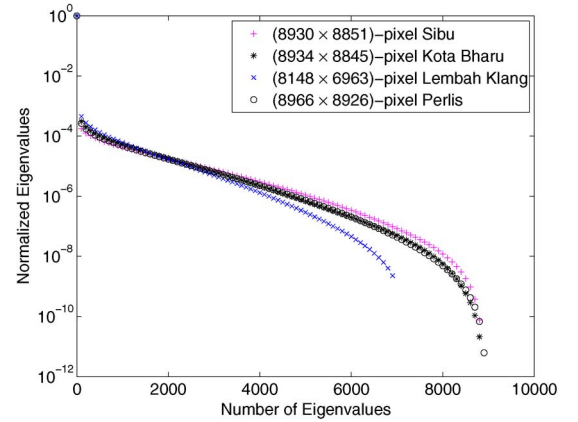


Fig. 2. Eigenvalue profile of  $R_X$ , generated from the full-size SAR images in Fig. 1.

Before reaching at the final form of the  $H_{\text{SDC}}$  estimator, it is worthy to note that, in similar way to time-domain signals [19], [26], the covariance matrix of an image has some of its eigenvalues small enough to be considered as zeros. To verify this key statement, four single-look images, shown in Fig. 1, of, respectively,  $8930 \times 8851$  pixels,  $8934 \times 8845$  pixels,  $8148 \times 6963$  pixels, and  $8966 \times 8926$  pixels are obtained from the Malaysian Remote Sensing Agency. The images are acquired by RADARSAT-1 which operates at C-band with a frequency of 5.3 GHz and has spatial resolution ranges from 8 to 100 m. The images in Fig. 1(a)–(c) represent mostly vegetation areas, whereas the Lembah Klang image in Fig. 1(d) represents mostly urban area. The eigenvalues of the four SAR images in Fig. 1 are calculated and depicted against their number in Fig. 2. The results clearly indicate that some of the eigenvalues of the considered images are too small in comparison to their largest values and practically can be set to zero without affecting the distribution of their powers in the Euclidean space. This means that the number of the basis vectors of the noise-free images is generally smaller than the dimension of their vectors.

The fact that some of the eigenvalues of matrix  $R_X$  are close to zero indicates that the energy of the clean image is distributed among a subset of its coordinates, and the signal is confined to a subspace of the noisy Euclidean space. Since all noise eigenvalues are strictly positive, the noise fills in the entire vector space of the noisy image. Hence, the vector space of the noisy image is composed of a signal-plus-noise subspace

and a complementary noise subspace. The signal-plus-noise subspace or simply the signal subspace comprises vectors of the clean image as well as of the noise process. On the other hand, the noise subspace contains vectors of the noise process only. In order to implement the concept of signal subspace and noise subspace with  $H_{\text{SDC}}$  in (21) for further enhancement, we establish in the subsequent section the relationship between the eigendecomposition and the oriented energy.

### B. Conceptual Relations Between Eigendecomposition and Oriented Energy

Consider a square matrix  $A$  of dimension  $m \times m$ . The column of  $A$  is considered to form an indexed set of  $m$  vectors, denoted by  $\{\mathbf{a}_k\}$ ,  $k = 1, 2, \dots, m$ . An  $M$ -dimensional vector  $\mathbf{q}$  and the direction it represents in a vector space are used as synonyms.

**Theorem 1: Energy of a Vector Sequence:** Consider a sequence of  $m$ -vectors  $\{\mathbf{a}_k\}$ ,  $k = 1, 2, \dots, m$  and an associated real  $m \times m$  matrix  $A$ . Its total energy  $E[A]$  is defined via Frobenius norm of the  $m \times m$  matrix  $A$

$$E[A] = \|A\|_F^2 = \sum_{i=1}^m \sum_{j=1}^m a_{ij}^2. \quad (22)$$

**Definition 1: Oriented Energy:** Let  $A$  be an  $m \times m$  matrix, and denote its  $m$ -column vectors as  $\{\mathbf{a}_k\}$ ,  $k = 1, 2, \dots, m$ . For the indexed vector set  $\{\mathbf{a}_k\}$  of  $m$ -vectors  $\mathbf{a}_k$  and for any unit vector  $\mathbf{q}$ , the energy  $E_q$  measured in direction  $\mathbf{q}$  is defined as [30]

$$E_q[A] = \sum_{k=1}^m (\mathbf{q}^T \cdot \mathbf{a}_k)^2. \quad (23)$$

In a general form, the energy  $E_Q$  measured in a subspace  $Q \subset \mathbb{R}^m$  can be expressed as

$$E_Q[A] = \sum_{k=1}^m \|P_Q(\mathbf{a}_k)\|^2 \quad (24)$$

where  $P_Q(\mathbf{a}_k)$  is the orthogonal projection of  $\mathbf{a}_k$  into subspace  $Q$  and  $\|\cdot\|$  denotes the Euclidean norm. Equations (23) and (24) basically mean that the oriented energy of a vector sequence  $\mathbf{a}_k$ , measured in the direction of  $\mathbf{q}$  in subspace  $Q$ , is the energy of the signal, projected orthogonally onto the vector  $\mathbf{q}$ . In order to make use of the concept of signal subspace and noise subspace in model matrix  $H_{\text{SDC}}$ , we will establish in the following section the relationship between eigendecomposition and the concept of oriented energy distribution.

**Theorem 2: Symmetric EVD:** Any real symmetric matrix  $A \in \mathbb{R}^{m \times m}$  can be decomposed as

$$A = U \Delta U^T = \sum_{i=1}^m \delta(i) \cdot \mathbf{u}_i \cdot \mathbf{u}_i^T \quad (25)$$

where  $U$  is a square orthogonal matrix of eigenvectors  $[\mathbf{u}_1, \mathbf{u}_2, \dots, \mathbf{u}_m]$  and  $\Delta$  denotes a diagonal matrix of eigenvalues  $[\Delta = \text{diag}(\delta_1, \delta_2, \dots, \delta_m)]$ .

*Proof:* A proof of Theorem 2 is given in [31].

Define the unit ball UB in  $\mathbb{R}^m$  as

$$\text{UB} = \{\mathbf{q} \in \mathbb{R}^m \mid \|\mathbf{q}\|_2 = 1\}. \quad (26)$$

**Theorem 3:** Consider a sequence of  $m$  vectors  $\mathbf{a}_k$ ,  $k = 1, 2, \dots, m$  and the associated  $m \times m$  matrix  $A$ . With the eigendecomposition of  $A$  defined in (25), we have

$$E_{\mathbf{u}_i}[A] = \delta_i. \quad (27)$$

$\forall \mathbf{q} \in \text{UB} : \text{if } \mathbf{q} = \sum_{i=1}^m \gamma_i \cdot \mathbf{u}_i$ , where  $\gamma_i$  is a scalar, then

$$E_{\mathbf{q}}[A] = \sum_{i=1}^m \gamma_i \cdot \delta_i. \quad (28)$$

*Proof:* Trivial from Theorem 2.

Equation (27) simply means that the oriented energy measured in the direction of the  $i$ th eigenvector of  $A$  is equal to the  $i$ th eigenvalue, whereas (28) indicates that the energy in an arbitrary direction of  $\mathbf{q}$  is a linear combination of “orthogonal” oriented energies associated with the eigenvectors.

With the aid of Theorem 3 and eigenvalue decomposition (EVD), we can easily obtain the direction and magnitude of extremal energy in signal-plus-noise subspace and minimal energy in noise subspace.

**Corollary 1:** Let matrix  $A$  be a rank-deficient matrix with rank  $r$ . Under the assumption of Theorem 3, we have

$$1. \max_{\mathbf{q} \in \text{UB}} E_{\mathbf{q}}[A] = E_{\mathbf{u}_1}[A] = \delta_1 \quad (29)$$

$$2. \min_{\mathbf{q} \in \text{UB}} E_{\mathbf{q}}[A] = E_{\mathbf{u}_m}[A] = \delta_m \quad (30)$$

$$3. \max_{Q^r \subset \mathbb{R}^m} E_{Q^r}[A] = E_{S_U^r}[A] = \sum_{i=1}^r \delta_i \quad (31)$$

$$4. \min_{Q^r \subset \mathbb{R}^m} E_{Q^r}[A] = E_{(S_U^{m-r})^\perp}[A] = \sum_{i=m-r+1}^m \delta_i \quad (32)$$

where “max” and “min” denote operators maximizing and minimizing, overall  $r$ -dimensional subspace,  $Q^r$  of the space  $\mathbb{R}^m$ .  $S_U^r$  is the  $r$ -dimensional principal subspace (signal subspace) of matrix  $A$ , and  $(S_U^{m-r})^\perp$  denotes the orthogonal complement of  $S_U^r$ .

*Proof:* Properties (29)–(32) are derived directly from the eigendecomposition Theorem 2 and its relationship to oriented energy distribution as stated in Theorem 3.

Properties (29) and (30) specifically show the relationship between the EVD to the maxima and minima of the oriented energy distribution. In fact, it can be shown that the extrema occur at the first eigenvector and the minima occur at the last one.

The  $r$ -principal subspace  $S_U^r$ , spanned by  $r$ -leftmost eigenvectors, is the one that senses a maximal oriented energy as shown in (31). Properties (31) and (32) indicate that the orthogonal decomposition of the energy via eigendecomposition is canonical in the sense that it allows the principal (signal) subspace to be found based on maximal energy criteria. On the other hand, the noise subspace  $S_U^{m-r}$  is the one that is spanned by  $(m - r + 1)$ -rightmost eigenvectors that sense the minimal energy. This decomposition of Euclidean space, as direct sum of a space of maximal and minimal energies for a given data matrix  $A$ , leads to very interesting reduced-rank model and noise cancellation technique.

### C. Optimum Estimator Using Principal Subspace

Having established the link between the maximal oriented energy and the signal subspace as well as between the minimal energy and the noise subspace, we are in a position to improve the form of  $H_{SDC}$  in (21) by removing the noise subspace and estimating the clean image from the remaining signal subspace. Consider the covariance matrix of the clean image  $R_X$  as a rank deficient matrix with rank  $r$ . Assume matrix  $U \in \mathbb{R}^{m \times m}$  as the eigenvectors of  $R_X$ . Let us partition  $U$  into  $r$  vectors that span the signal subspace and  $(m - r)$  vectors that span the noise subspace. Using EVD, this can be expressed as

$$\begin{aligned} R_X &= U_X \Delta_X U_X^T \\ &= (U_1 \ U_2) \begin{pmatrix} \Delta_{X1} & 0 \\ 0 & 0 \end{pmatrix} \begin{pmatrix} U_1^T \\ U_2^T \end{pmatrix} \end{aligned} \quad (33)$$

where  $U_1$  is an  $(m \times r)$ -matrix,  $U_2$  is an  $m \times (m - r)$ -matrix, and  $\Delta_{X1} = \text{diag}(\delta_1, \delta_2, \dots, \delta_r)$ . Since the noise is considered to be white, the noise covariance matrix can be expressed as  $R_N = v_n^2 I_m$ , and the eigenvectors  $U$  are unaffected by the constant diagonal perturbation [26]. Using the effect of small perturbation on data matrix, the eigendecomposition of  $R_Y$  is expressed as

$$\begin{aligned} R_Y &= U_Y \Delta_Y U_Y^T \\ &= (U_1 \ U_2) \begin{pmatrix} \Delta_{X1} + v_n^2 I_r & 0 \\ 0 & v_n^2 I_{m-r} \end{pmatrix} \begin{pmatrix} U_1^T \\ U_2^T \end{pmatrix}. \end{aligned} \quad (34)$$

From (33) and (34), it is clear that the eigenvectors for the clean and noisy covariance matrices are the same. On the other hand, the eigenvalues of  $R_Y$  are equal to the sum of  $\Delta_X$  and noise variance  $v_n^2$ ; hence,  $\Delta_X$  can be estimated directly from (34) provided that the value of  $v_n^2$  is known. This results in the following form for the linear estimator in (21):

$$H_{SDC} = U_1 \Delta_{X1} (\Delta_{X1} + \mu v_n^2 I)^{-1} U_1^T \quad (35)$$

where  $\Delta_X^{(i)} = \Delta_Y^{(i)} - v_n^2$ . To implement (35) for  $H_{SDC}$ , the rank of the signal subspace  $r$  and the optimum value of the Lagrange multiplier  $\mu$  are considered *a priori* known. In the subsequent two sections, we discuss the optimum values of  $r$  and  $\mu$ .

### D. Estimation of Noise Variance

In [32], Moor gives a detailed analysis on the validity of singular value decomposition (SVD) in subspace-based methods in dealing with additive white noise. One of the established algebraic and geometric conditions is that there is a distinct gap between the smallest singular value of the signal subspace and the largest singular value of the noise subspace. Theoretically, the last  $(n - r)$ -trailing end of the smallest singular is similar and equal to the noise standard deviation value. Thus, the noise variance can be estimated as

$$v_n^2 = \frac{1}{n - r} \sum_{i=r+1}^n \alpha_{Y,i}^2 \quad (36)$$

where  $\alpha_{Y,i}$  is the  $i$ th singular value of the noisy image  $Y$ .

### E. Rank Estimation of Matrix A

Consider that matrix  $A \in \mathbb{R}^{m \times n}$  represents an image, and it is needed to find its best approximation in terms of a reduced-dimension matrix  $B$ . A commonly used method for such purpose is to approximate  $A$  with a matrix of lower rank. The mathematical formulation of the optimal rank- $p$  approximation of  $A$ , under the Frobenius norm, is a problem of finding a lower ranked matrix  $B \in \mathbb{R}^{m \times n}$  with  $\text{rank}(B) = p$  such that

$$B = \arg \min_{\text{rank}(B)=p} \|A - B\|_F^2. \quad (37)$$

Matrix  $B$  can be obtained by computing the SVD of  $A$ , as stated in the following theorem [31].

**Theorem 4:** Let the SVD of  $A \in \mathbb{R}^{m \times n}$  be

$$A_{m \times n} = U_{m \times m} \cdot S_{m \times n} \cdot V_{n \times n}^T \quad (38)$$

where  $U$  and  $V$  are real orthonormal, and the matrix

$$S = \text{diag}(\alpha_1, \dots, \alpha_r, 0, \dots, 0) \quad (39)$$

where  $\alpha_1 \geq \alpha_2 \geq \dots \alpha_r > \alpha_{r+1} = \dots = \alpha_n = 0$  and  $r = \text{rank}(A)$ . Then

$$\sum_{i=p+1}^r \alpha_i^2 = \min_{\text{rank}(B)=p} \|A - B\|_F^2, \quad 1 \leq p \leq r. \quad (40)$$

The minimum is achieved with  $B = \text{best}_p(A)$ , where

$$\text{best}_p(A) = U_p \cdot \text{diag}(\alpha_1, \dots, \alpha_p) \cdot V_p^T. \quad (41)$$

Here,  $U_p$  and  $V_p$  are the matrices formed by the first  $p$  columns of  $U$  and  $V$ , respectively.

This means that, for any approximation  $B$  of  $A$ , the term  $\|A - B\|_F$  is the reconstruction error, and by Theorem 4,  $B = U_p \cdot \text{diag}(\alpha_1, \dots, \alpha_p) \cdot V_p^T$  has the smallest reconstruction error among all of the rank- $p$  approximations of  $A$ .

Using this approximation, each  $m$ -dimensional column  $a_i$  of  $A$  can be approximated as  $a_i \approx U_p a_i^L$ , for some  $a_i^L \in \mathbb{R}^p$ . Since  $U_p$  has orthonormal columns

$$\|U_p a_i^L - U_p a_j^L\| = \|a_i^L - a_j^L\| \quad (42)$$

which basically means that the Euclidean distance between two vectors is preserved under the orthogonal projection. It follows that

$$\|a_i - a_j\| \approx \|U_p a_i^L - U_p a_j^L\| = \|a_i^L - a_j^L\|. \quad (43)$$

Since each  $a_i$  is approximated by  $U_p a_i^L$ , where  $U_p$  is common for every  $a_i$ , hence we only need to store  $U_p$  and  $\{a_i^L\}_{i=1}^n$  for all approximation. With  $U_p \in \mathbb{R}^{m \times p}$  and  $a_i^L \in \mathbb{R}^p$ , for  $i = 1, \dots, n$ , it would require  $(mp + np)$  scalars to store the reduced representations. In this case, for original image matrix  $A$  of size  $m \times n$ , the compression ratio  $C_r$  using the rank- $p$  approximation is [33], [34]

$$C_r = \frac{mn}{(m+n)p}. \quad (44)$$

Now, let us consider the problem of finding the rank of a noisy image  $Y$  that follows the additive noise model in (11).



Fundamentally, the clean matrix  $X$  has a reduced rank  $r \leq \min(m, n)$ , whereas the noise matrix  $N$  has full rank. The singular values of  $Y$  are given by

$$S = \text{diag}(\alpha_1, \dots, \alpha_n) \quad (45)$$

where  $\alpha_1 \geq \alpha_2 \geq \dots \geq \alpha_r > \alpha_{r+1} \geq \dots \geq \alpha_n \geq 0$  and  $(\alpha_{r+1}, \dots, \alpha_n)$  are usually small but not necessarily zero. One approach to estimate the rank  $r$  of the matrix  $Y$  from the computed singular values is to have a tolerance  $\tau$  and a convention that  $Y$  has “numerical” rank  $r$  if its singular values satisfy the following criteria [31]:

$$\alpha_1 \geq \alpha_2 \geq \dots \geq \alpha_r > \tau \geq \alpha_{r+1} \geq \dots \geq \alpha_n. \quad (46)$$

Different statistical models were proposed for the selection of the threshold bounds  $\tau$ . Among the best-known models are the finite precision model, the i.i.d. random model, and the column random model [35]. In this paper, the selected threshold bound is based on the i.i.d. random model given by [35]

$$c \leq \tau \leq \sqrt{(mn)c} \quad (47)$$

where  $2v_n \leq c \leq 2.6v_n$  and  $v_n$  is the standard deviation of the noise. The threshold bound in (47) is derived using the perturbation theory of singular values and a statistical significance test. Based on (47), the obtained threshold bound is a function of matrix dimension, noise variance, and predefined statistical level of significance.

#### F. Optimum Value of the Lagrange Multiplier

To find the best  $\mu$  value for SDC, a mosaic image composed of synthetic patterns, specimens from Broadatz texture set, and two optical remote sensing images is created. The image is made up of four quarters, each of  $256 \times 256$  pixels, and is shown in Fig. 3(a). The first quarter represents synthetically created homogenous regions, the second quarter is an optical image showing a mountainous area, the third quarter is another optical image showing an airport area, and the fourth quarter is taken from Broadatz texture set. The test image is corrupted with speckle noise of variance that extends from 0.02 to 0.2, and the SDC is run with  $\mu$  ranging between 10 and 300. The signal-to-noise ratio (SNR) value calculated as

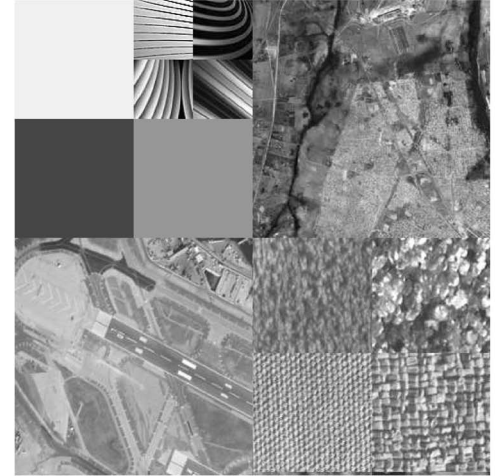
$$\text{SNR}_{\text{dB}} = 10 \log_{10} \frac{\bar{v}_X^2}{\text{MSE}} \quad (48)$$

where MSE represents the mean-square error, given by

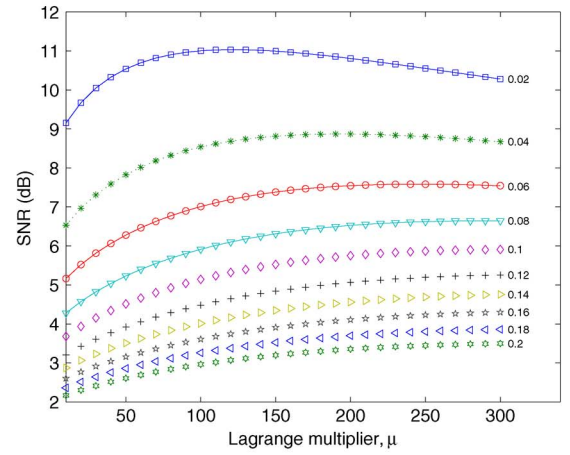
$$\text{MSE} = \frac{1}{mn} \sum_{i=1}^m \sum_{j=1}^n (X(i, j) - Y(i, j))^2 \quad (49)$$

is used to indicate the denoising effect of the SDC. The results are shown in Fig. 3(b).

The results in Fig. 3(b) show that the SDC is not too sensitive to the selected value of the Lagrange multiplier. In particular, the despeckle effect of the SDC, measured in terms of the SNR, shows improvement by only 1-1.5 dB, for the different values of the noise variance, as the Lagrange multiplier varies from 5 to



(a)



(b)

Fig. 3. (a) Mosaic test image. (b) SNR of the mosaic image in (a) obtained at different  $\mu$  values.

300. In general, the results in Fig. 3(b) show better SNR values for higher values of the Lagrange multiplier. However, it should be noted that the high value of  $\mu$  may result in oversmoothed images and may cause loss of details. Consequently, the rule of selecting  $\mu$  is that, for noise variance less than 0.06,  $\mu$  should be selected within the range from 50 to 100 and, with noise variance greater than 0.06, it should be selected around 200.

#### G. Implementation of Signal Subspace Approach for Uncorrelated Speckle Noise

- 1) Apply the homomorphic transformation to the noisy image  $Y_l = \log(G)$ .
- 2) Estimate the noise variance  $v_n^2$ .
- 3) Compute the dimension of signal subspace  $r$ .
- 4) Using the estimated  $r$  in step 3, apply eigendecomposition on  $R_{Y_l}$ ; then, extract the basis vectors of signal subspace  $U_1$  and their related eigenvalues  $\Delta_X^{(i)} = \Delta_Y^{(i)} - v_n^2$ .
- 5) Select  $\mu$  according to the rule in Section III-F; then, compute the optimum linear estimator

$$H_{\text{SDC}} = U_1 \Delta_{X1} (\Delta_{X1} + \mu v_n^2 I)^{-1} U_1^T. \quad (50)$$

- 6) Compute the clean image  $\hat{X}_l = H_{\text{SDC}} \cdot Y_l$ .

- 7) Reverse the homomorphic effect by taking the exponential of  $\hat{X}_l$  as follows:

$$\hat{X} = 10^{\hat{X}_l}. \quad (51)$$

- 8) Apply bias adjustment according to Section II-A.

#### IV. RESULTS AND DISCUSSIONS

This section is divided into two parts. In the first part, the performance of the SDC as a function of the size of the image, as well as its capability in representing real SAR images, is investigated. In the second part, the performance of the proposed SDC technique is compared with both Lee [4] and the homomorphic wavelet filter [20], [21] using synthetic images and real SAR images. Lee filter is implemented with  $7 \times 7$  window size, and the homomorphic wavelet is used with the Daubechies length-eight filter and a  $7 \times 7$  window. The SDC is implemented as in Section III-G. The rank values of the different images are calculated using the method outlined in Section III-E, and the Lagrange multiplier is selected using the rule set in Section III-F. The noise variance is estimated using (36).

##### A. Performance of SDC With the Size of the Image

Since the proposed SDC is a global technique that operates directly on the whole image, it is essential to investigate its performance with the size of the image. This experiment is conducted by adding speckle noise to the synthetic image in Fig. 4(a) at different noise levels and by calculating the PSNR gain from the despeckled image. The PSNR in decibels is defined as

$$\text{PSNR} = 20 \log_{10} \left( \frac{256}{\sqrt{\text{MSE}}} \right) \quad (52)$$

where the MSE is calculated as in (49).

The results obtained from the average values of 100 trials for the mix image in Fig. 4(a) are shown in Fig. 4(b). Here, the image size is varied from  $500 \times 500$  to  $10 \text{ k} \times 10 \text{ k}$  pixels. The results indicate better performance by the SDC with the growing size of the image. In general, the SDC performance improves by approximately 1.5 dB when the size increases from  $500 \times 500$  to  $1000 \times 1000$  pixels and by 0.6 dB when the size increases from  $1000 \times 1000$  to  $2000 \times 2000$ . Similar results are obtained with portrait images, like Lena, Barbara, and boat. Generally speaking, the better performance of the SDC with the increased size of the image is mainly attributed to the improved structure of the estimated noise covariance matrix in terms of its diagonality. Close observation of the noise covariance matrix shows nonzero off-diagonal values when the size of the image is small and closer structure to diagonal as the image grows in size.

##### B. Capability of SDC in SAR Image Representation

To test the capability of the SDC in preserving SAR image details with  $r$ -dimensional principal subspace, the algorithm is

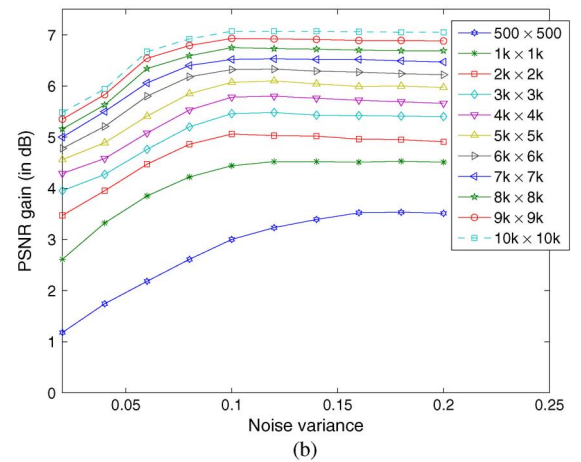
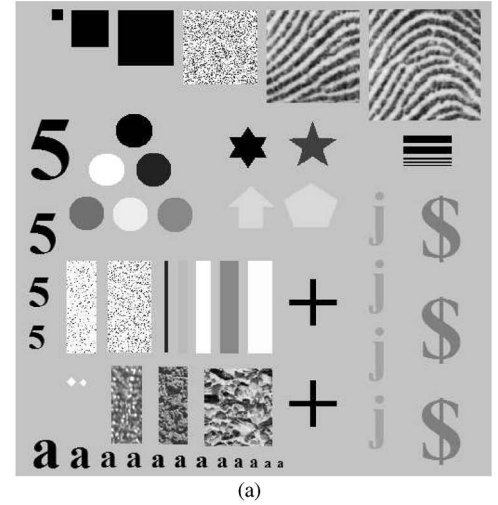


Fig. 4. (a) Mix test image. (b) PSNR gain for the different sizes of the test image in (a), obtained at various noise levels.

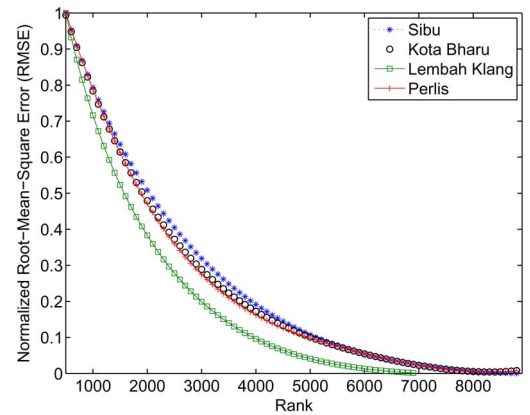


Fig. 5. Reconstruction error of SAR images in Fig. 1 at different rank values.

run with the four images in Fig. 1, and the root-mean-square error (RMSE) metric is used to indicate its performance. In this experiment, the rank values are increased from 500 to around 8000 with a step size of 100, and the RMSE values are calculated and shown in Fig. 5. The results in Fig. 5 clearly show the capability of the SDC in preserving the details of SAR images with a reduced-rank model. It is quite clear that the SDC can represent the four SAR images with an RMSE of  $< 0.1$  using rank values of  $r \approx 4000$  for the mostly urban area of the



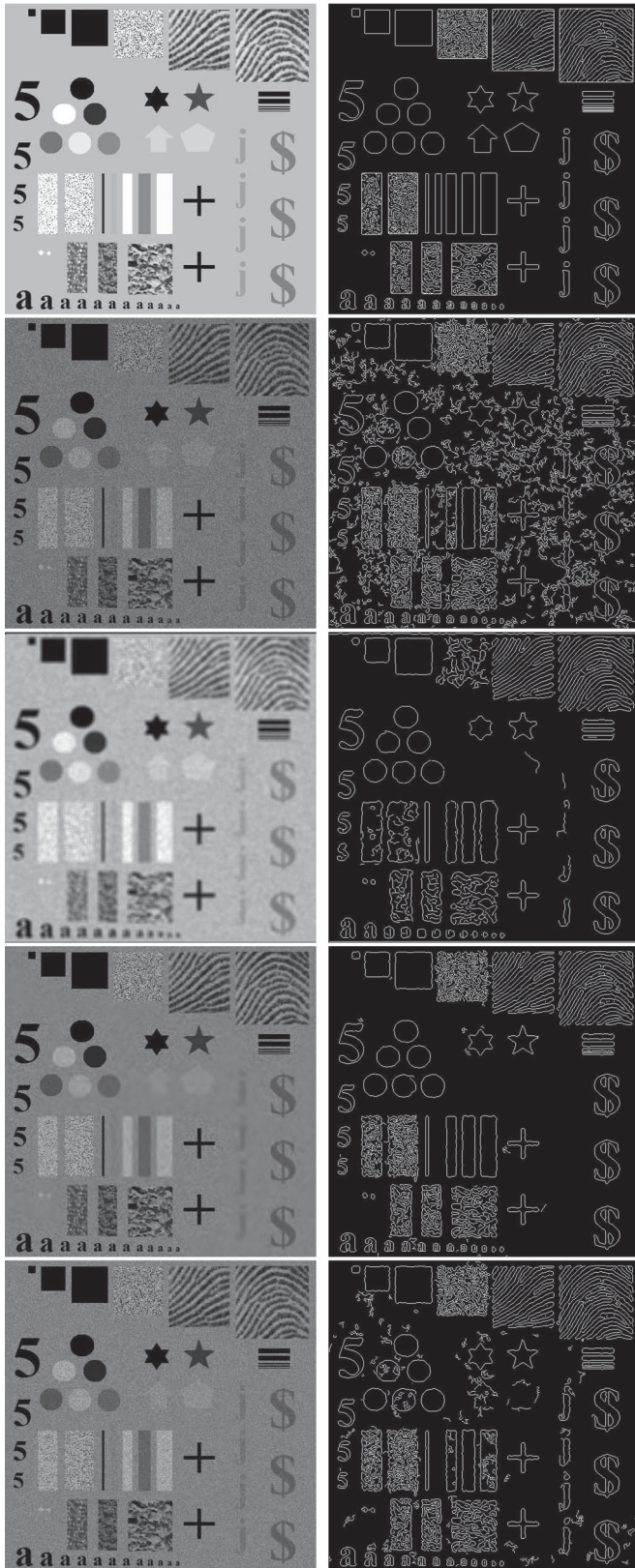


Fig. 6. Edge maps of the despeckled images of the mix image in Fig. 4(a) corrupted by a noise variance of 0.07. From top to bottom: noise-free image, noisy image, Lee filter, homomorphic wavelet, and SDC.

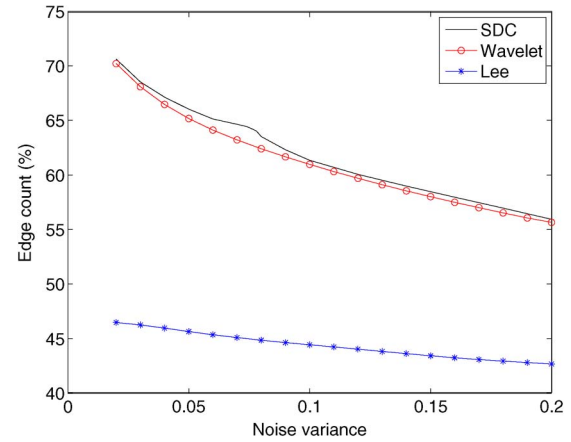


Fig. 7. Edge counts (in percentage) in the despeckled images.

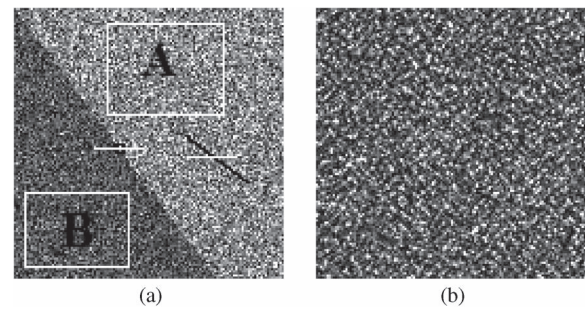


Fig. 8. Synthetically generated three-look test images.

### C. Evaluation of SDC Performance in Simulated Speckle Noise Scenario

In this experiment, the capability of the SDC technique in preserving the edges of images corrupted with speckle noise is tested and compared with Lee and the homomorphic wavelet. The edge count metric (EC) formulated as the ratio between the total number of actual edge pixels  $I_r$  in a reconstructed image and the total number of edge pixels  $I_i$  in the noise-free image is used to indicate the performance of the three techniques. The EC values are obtained by implementing a Canny filter on both noise-free and despeckled images for edge detection. The correctly detected edges are then obtained by comparing the edge map of the despeckled image with the edge map of the clean image and by counting the rightly detected edges.

In this experiment, the given image in Fig. 4(a), which is made up of textured images, geometrical shapes, and some alphabets with different contrast values, is used to assess the capability of the SDC, Lee, and homomorphic wavelet in preserving the edges in the despeckled image. Initially, the ground truth image is produced by applying a Canny edge detector to the noise-free image in Fig. 4(a). The edge map of the clean image is shown in Fig. 6. From the edge map of the noise-free image in Fig. 6, the exact number of edges in the image  $I_i$  is obtained. Next, the noise-free image is corrupted with speckle noise at various variance values that extend from 0.02 to 0.2. The SDC, Lee, and homomorphic wavelet are used to despeckle the noise in the noisy image; then, the Canny edge detector is applied to find the edges in the images. The number of correctly detected edges in the despeckled images  $I_r$  is calculated, and the EC values are obtained and depicted against noise variance in Fig. 7.

Lembah Klang image and  $r \approx 5000$  for the other three mostly vegetation images. The results also show the little dependence by the SDC on the contents of the SAR images.

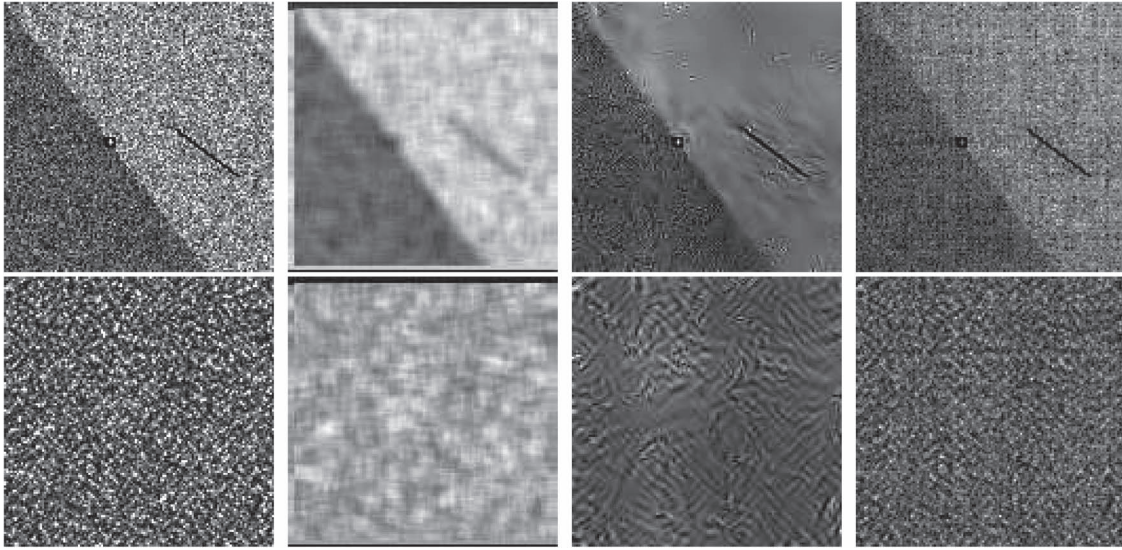


Fig. 9. Restoration of (top) image (a) and (bottom) image (b) of Fig. 8. From left to right: original, Lee filter, homomorphic wavelet filter, and SDC filter.

The results in Fig. 7 demonstrate almost similar capability by the SDC and the homomorphic wavelet in preserving the edges in the despeckled image. On the other hand, the results show the better capability of the SDC and the homomorphic wavelet in preserving the edges in the despeckled image in comparison to the Lee filter. In particular, the SDC and the wavelet outperform Lee ( $7 \times 7$ ) by nearly 25% at the small values of noise variance and by around 15% at the high values of noise variance. Of course, implementing Lee with smaller windows will improve its performance, but it remains inferior to SDC and wavelet.

For more insights into the edge preservation of the considered techniques, the noise-free image in Fig. 6 is corrupted with a speckle noise of variance of 0.07. The despeckled images by Lee, homomorphic wavelet, and SDC along with their edge maps generated using the Canny filter with threshold set at 0.15 and Gaussian kernel width of 1 are shown in Fig. 6. Close examination of the edge maps in Fig. 6 shows that the SDC retains more features in the textured area and suffers less blurring effect than Lee and the homomorphic wavelet. In addition, the SDC is able to map out the edges of almost all regions, except the low contrast ones of the arrow and the pentagon. However, since the SDC is less efficient than Lee and wavelet in smoothing out the background noise, more spurious edges appeared in the edge map. On the other hand, the wavelet is good in removing the background noise, but in doing so, it blurred out all of the “j” alphabets and the low contrast region of the arrow and the pentagon. Contrary to the homomorphic wavelet, Lee filters show a good capability in detecting the edges in the region of the low contrast “j” alphabets and show less spurious edges than the SDC over the image, but the blurring effect of the used  $7 \times 7$  window results in poor edge reconstruction in the textured area.

#### D. Evaluation of SDC Performance Using Synthetic Images Generated Using Controlled Statistic

In this experiment, we consider the two synthetically generated three-look test images that are shown in Fig. 8. Fig. 8(a) comprises two stationary areas with delta correlated speckle,

TABLE II  
NORMALIZED NOISE VARIANCE IN THE DENOISED IMAGES OF FIG. 8

3-Look	Original	Lee	Wavelet	SDC
Region A of Image (a)	0.36	0.01	0.15	0.15
Region B of Image (a)	0.35	0.01	0.14	0.14
Image (b)	0.48	0.01	0.08	0.19

TABLE III  
MEAN PRESERVATION IN THE DENOISED IMAGES OF FIG. 8

3-Look	Original	Lee	Wavelet	SDC
Region A of Image (a)	72.69	72.55	58.15	61.95
Region B of Image (a)	72.76	72.79	59.66	63.55
Image (b)	88.45	88.41	63.58	68.48

in addition to a point target that appears at the center of the line separating the two areas, whereas Fig. 8(b) contains  $K$ -distributed exponential cosine clutter. The denoised versions of the speckled images in Fig. 8 by the SDC, wavelet, and Lee filters are shown in Fig. 9.

The assessment of the filters in the stationary area of the images in Fig. 8 is based on the value of normalized variance and the preservation of autocorrelation. The normalized variance is given by

$$\frac{\text{var}}{\text{mean}^2} = \frac{\frac{1}{mn} \sum_{i=1}^m \sum_{j=1}^n (X(i, j) - \bar{X})^2}{\bar{X}^2} \quad (53)$$

where  $\bar{X}$  corresponds to the mean value of the pixel, and the autocorrelation for  $m \times n$  image  $X$  is given as [36]

$$\rho(x, y) = \frac{\frac{1}{(m-|x|)(n-|y|)} \sum_i \sum_j X(i, j) X(i+x, j+y)}{\frac{1}{mn} \sum_{i=1}^m \sum_{j=1}^n X(i, j)^2} \quad (54)$$

where  $X(i, j)$  is the gray value of pixel  $(i, j)$ .

In general, the lower normalized variance values in the filtered image indicate better speckle suppression, and the close autocorrelation profile to the original image indicates better texture preservation.



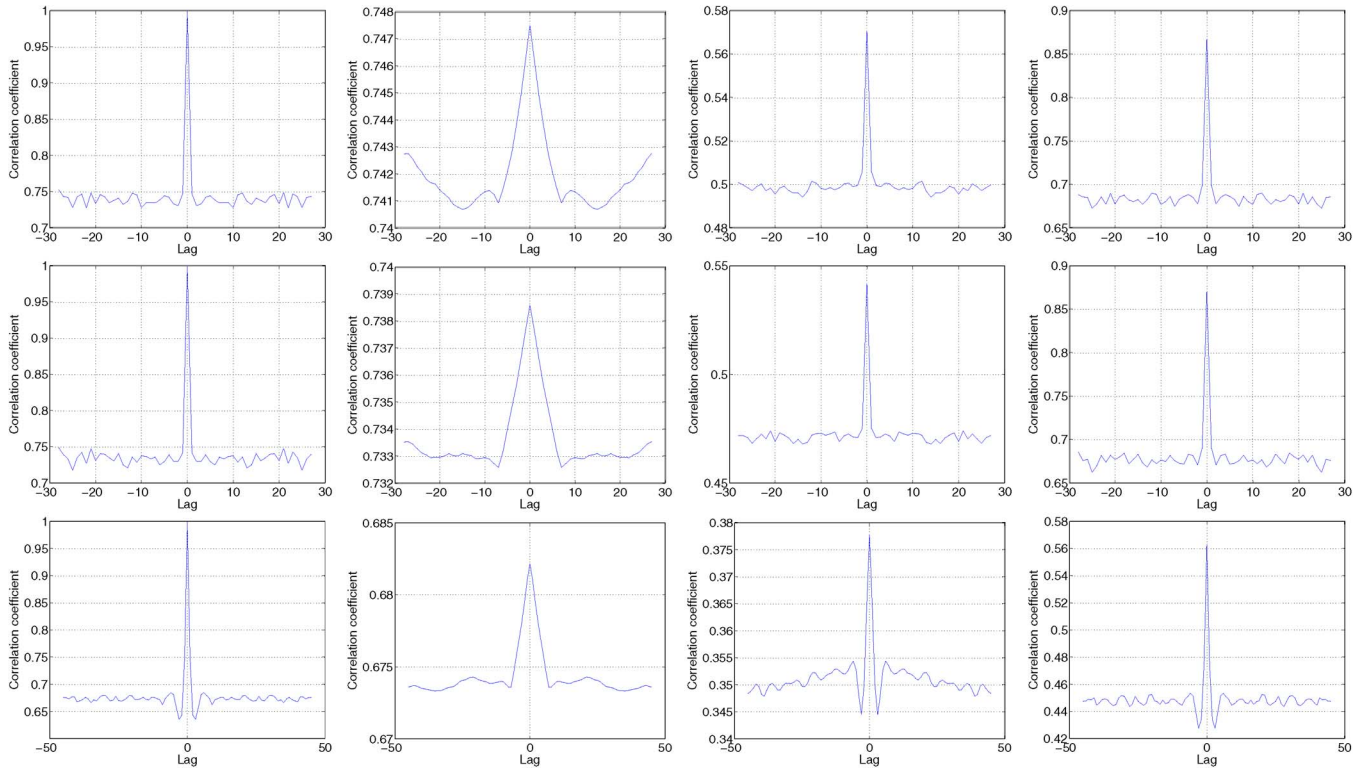


Fig. 10. Autocorrelation profiles for (top) region A of image (a), (middle) region B of image (a), and (bottom) image (b) of Fig. 8. From left to right: original, Lee filter, homomorphic wavelet filter, and SDC filter.

In Fig. 8(a), the normalized variance and the autocorrelation coefficient are calculated over two selected regions, namely, A and B, whereas in Fig. 8(b), the two metrics are calculated over the whole image. The variances of the three regions are calculated before and after denoising the images using SDC, Lee, and wavelet filters, and the results are included in Table II.

The results in Table II clearly show the better reduction of noise achieved by Lee to both wavelet and SDC over the three selected regions. However, in order to gain more insights into the performances, the denoised images of Fig. 8 by SDC, Lee, and wavelet are shown in Fig. 9. Visual inspection of the denoised image by Lee in Fig. 9 clearly shows that the achieved high noise reduction rate by the filter in Table II is mainly because of the blurry nature of the produced image at its output. The results in Table II also show a slightly better noise reduction achieved by wavelet in comparison to SDC over the three selected regions in Fig. 8. However, the wavelet denoised image in Fig. 9 demonstrates intensive presence of the ringing effects which act as smoothing artifacts and leads to noise variance reduction. In summary, SDC shows moderate noise variance reduction rate in comparison to Lee but with far less blurring effect and a comparable performance to wavelet, but with significantly less artifacts and better detail preservations. Moreover, as it is indicated by Donoho *et al.* [37], “estimates which are optimal from a mean-squared error point of view exhibit considerable, undesirable, noise induced structures—“ripples”, “blips”, and oscillations. Such noise-induced oscillations may give rise to interpretational difficulties.” We observed that such artifacts are indeed present, for instance, in the Lee-filtered image (as a consequence of the statistical technique

based on optimization of the mean squared error), whereas they are not present in the SDC implementation.

In addition to the noise reduction issue represented by the normalized variance, the capability of the various techniques in preserving the mean value is also tested and included in Table III. The results clearly show the better performance of Lee in preserving the mean values of the synthetically produced images in Fig. 8 than both SDC and wavelet and the slightly better performance of SDC to wavelet. This result is expected because of the averaging scheme in Lee which tends to maintain the mean value in the image.

In order to address the capability of the different algorithms in texture preservation in the denoised image, the autocorrelation of regions A and B in Fig. 8(a) and the autocorrelation of the whole image in Fig. 8(b) are calculated before and after speckle denoising and are depicted in Fig. 10.

The results in Fig. 10 clearly show the better preservation of the details of the original image by the wavelet and SDC in comparison to Lee. The two algorithms show a close autocorrelation profile to the original image than Lee which exhibits a wider profile than the original. This effect by Lee is expected since it acts as a low-pass (moving averaging) filter. On the other hand, the SDC shows a relatively better performance in terms of autocorrelation profile preservation than wavelet, especially in Fig. 8(b).

In order to show the capability of the algorithms in preserving lines, edges, and point targets, two transects are drawn through the point target and the line in Fig. 8(a). The intensity over the two transects of Fig. 8(a) is measured and depicted in Fig. 11. In Fig. 11(a), the intensity profile over the transect passing through the point target shows that SDC and wavelet



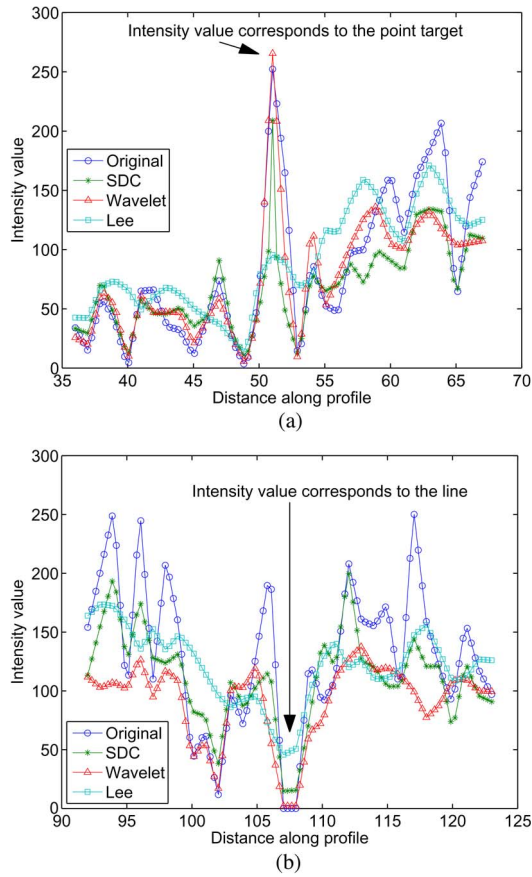


Fig. 11. Intensity profile for (a) transect through a point target and (b) transect through a line of Fig. 8(a).

are capable of preserving the point target, whereas Lee fails completely in showing it.

In Fig. 11(b), the intensity profile of transect through the line indicates that both SDC and wavelet managed to significantly clean the line and to preserve its radiometric edges. This is clear from the flat section of the intensity profile of the two filters in Fig. 11(b), which is proportional to the width of the region where the intersect pass through the line. The results in Fig. 11(b) also show that the Lee filter fails completely in detecting the line in Fig. 8(a). This is mainly because of the involved smoothing scheme with Lee which blurs the area around the object.

#### E. Evaluation of SDC Performance Using Real SAR Images

In this experiment, the performance of the proposed SDC algorithm is analyzed and compared with Lee and wavelet using intensity format three-look SAR image for Selangor area in Malaysia. The image is acquired by the RADARSAT-1 which operates at C-band with a frequency of 5.3 GHz and has spatial resolution ranges from 8 to 100 m. The image is shown in Fig. 12 and includes Klang port, urban areas, forests and jungle areas, and Strait of Malacca, in addition to paddy fields and bare soil areas.

In the first part of this experiment, two stationary areas are selected, including stationary with delta correlated speckle (bare soil and paddy fields), marked as region A, and stationary with exponential-cosine correlated clutter (forest area), marked

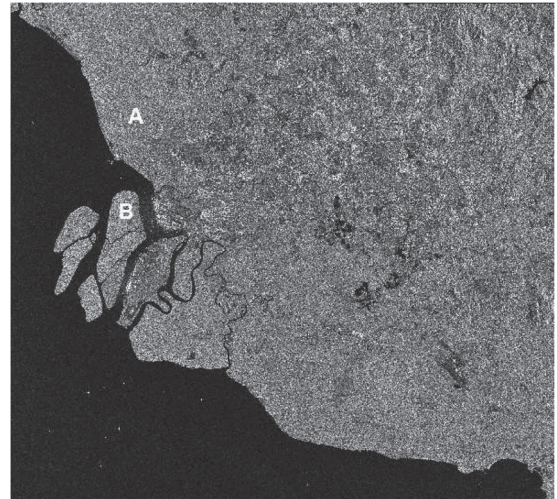


Fig. 12. 7090 × 7660 three-look SAR image of Selangor area. Courtesy of the Malaysian Remote Sensing Agency.

TABLE IV  
NORMALIZED NOISE VARIANCE IN THE DENOISED IMAGES OF FIG. 12

3-Look	Original	Lee	Wavelet	SDC
Paddy field/bare soil	0.35	0.01	0.10	0.13
Forest	0.35	0.02	0.06	0.10
6-Look	Original	Lee	Wavelet	SDC
Paddy field/bare soil	0.134	0.003	0.022	0.036
Forest	0.131	0.005	0.008	0.045

as region B. In order to assess the capability of the filters in reducing noise in the image, the variances are calculated over selected windows in regions A and B before and after denoising the original three-look image in Fig. 12 as well as a six-look version of it. Then, the amount of normalized variance is obtained and tabulated in Table IV. The results in Table IV for the real SAR areas are consistent with the results of the simulated images in Table II. However, for correct interpretation of the results in Table IV, Fig. 13 shows the selected areas of the original and denoised images in regions A and B.

In a similar way to Table II, the results in Table IV show significant noise reduction by Lee in comparison to SDC and wavelet and slightly better noise reduction by wavelet in comparison to SDC. However, Fig. 13 clearly shows that the better performance by Lee to SDC and wavelet is mainly because of the blurry nature of the produced image at its output and the relatively better performance by the wavelet to SDC is mostly motivated by the intensive presence of the ringing artifacts in its denoised image.

To gain more insights into the performance of the three considered techniques, their capabilities in preserving the characteristics of the original image are obtained through their autocorrelation profiles of a selected window in regions A and B and are shown in Fig. 14.

The results in Fig. 14 clearly show the better preservation of the textures of the original image by the SDC in comparison to Lee and wavelet. The SDC shows the close autocorrelation profile of the denoised image to the original one in terms of shape and better preservation of the unit impulse structure at zero lag value than Lee and wavelet. Furthermore, Fig. 14 shows that the autocorrelation profiles produced by Lee and wavelet represent a widened profiles at zero lag and largely

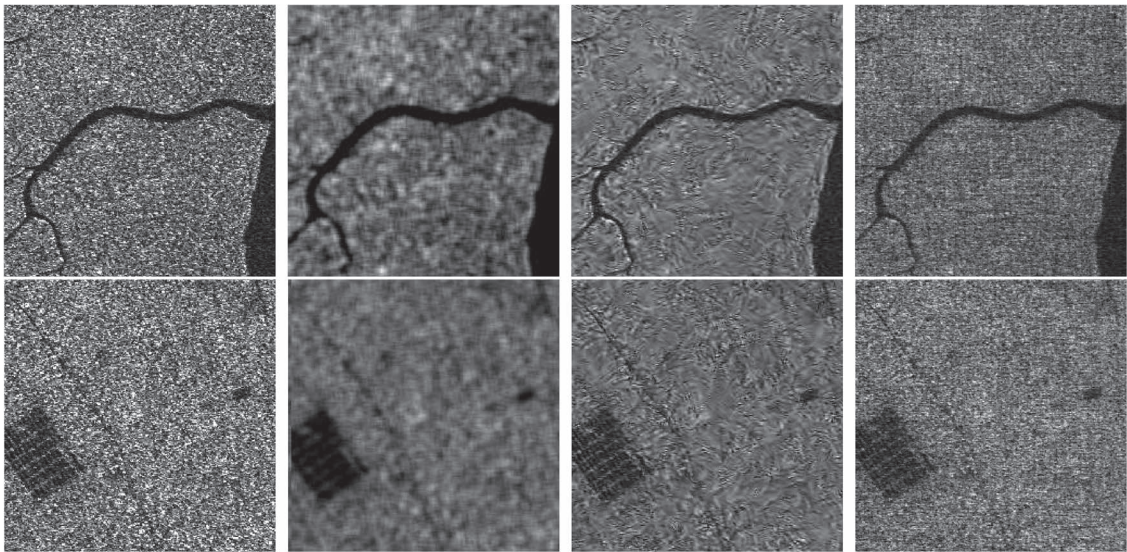


Fig. 13. Restoration of three-look forest area (top) and paddy field area (bottom) in Fig. 12. From left to right: original, Lee filter, homomorphic wavelet filter, and SDC filter.

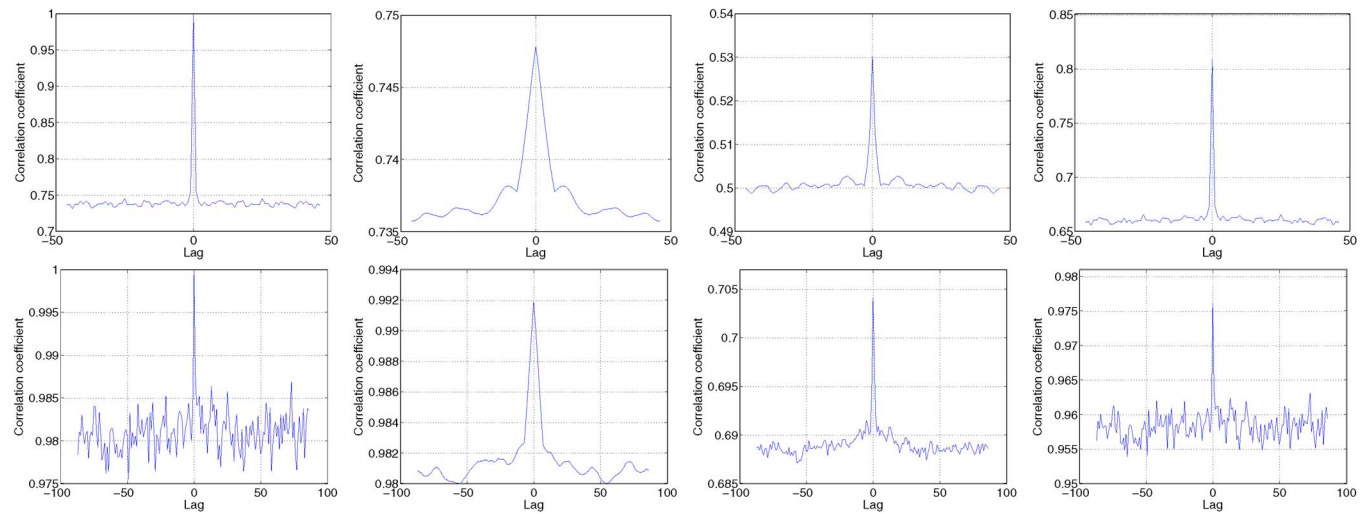


Fig. 14. Autocorrelation profile for (top) region A of image (a), (middle) region B of image (a), and (bottom) image (b) of Fig. 12. From left to right: original, Lee filter, homomorphic wavelet filter, and SDC filter.

TABLE V  
MEAN PRESERVATION IN THE DENOISED IMAGES OF FIG. 12

3-Look	Original	Lee	Wavelet	SDC
Paddy field/bare soil	88.00	86.86	73.86	75.55
Forest	82.97	82.85	68.27	71.36
6-Look	Original	Lee	Wavelet	SDC
Paddy field/bare soil	83.00	85.34	78.78	80.11
Forest	81.61	81.57	76.49	80.10

deviated profiles from the original at other lags, especially with Lee filter. This is mainly because of the low-pass filter effect of the smoothing scheme involved in Lee and the ringing artifacts in the wavelet.

In addition to their preservation of the autocorrelation coefficients, the capability of the algorithms in preserving the mean value of the original image is also tested with the images in Fig. 12 and is tabulated in Table V. The results indicate better capability by Lee in preserving the mean values of the three-

look and six-look images of Fig. 12 in comparison to SDC and wavelet and slightly better performance by SDC to wavelet.

In the second part of this experiment, the capability of the algorithms in preserving lines, edges, and point targets is assessed. The area near Klang port is selected, and two transects are drawn through an approximately point target (ship) and a hard target (roof). The selected area and the two transects are shown in Fig. 15. The intensity over the two transects is measured and depicted in Fig. 16. In Fig. 16(a), the intensity profile over the transect passing through the point target shows that SDC and wavelet are capable of preserving the point target, whereas Lee fails completely in showing it. On the other hand, the flat area in the intensity profile of SDC in Fig. 16(a) indicates that the filter, and contrary to the wavelet, is able to approximately detect the width of the ship through its better preservation of its radiometric edges. The results in Fig. 16(b) for the intensity profiles of the hard target at Klang port show similar results to the point target in Fig. 16(a). The



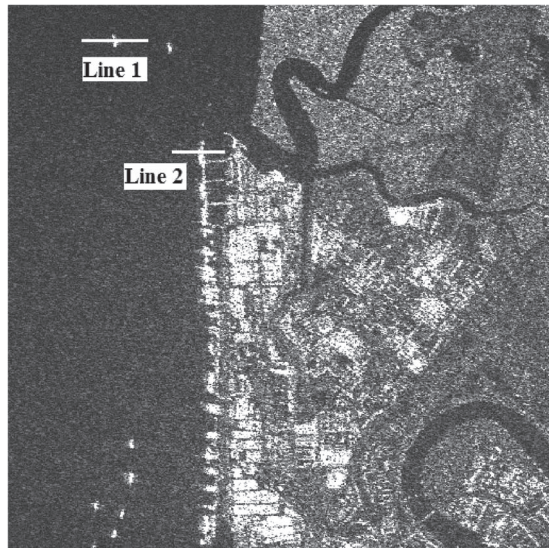


Fig. 15. Klang port area in Fig. 12.

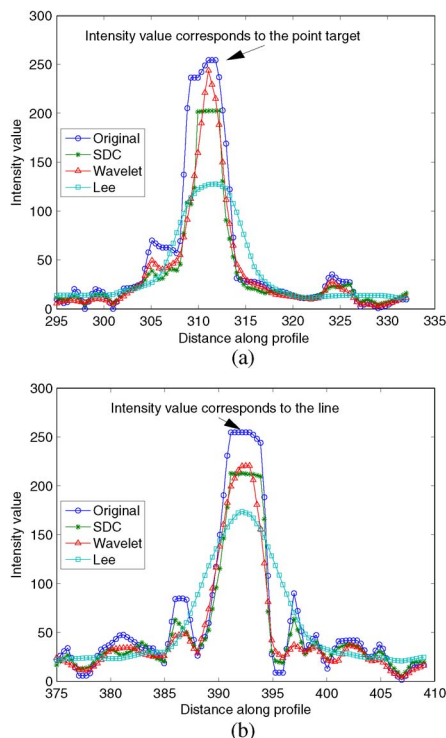


Fig. 16. Intensity profile for (a) transect through a point target and (b) transect through a line, of Fig. 15(a).

SDC and wavelet show better performance than Lee, and the SDC outperforms the wavelet in terms of its capability to detect better the width of the target as it is clear from the flat area of its intensity profile.

In the third experiment, the required computational times by Lee, SDC, and wavelet to process the SAR image of Fig. 12 are calculated and included in Table VI. The filters are ran on MATLAB platform using a computer with Intel(R) Xeon(R) 5607 @ 2.27-GHz processor and 8-GB RAM. The results in Table VI clearly show that the computational times of both SDC and wavelet are almost similar and less by nearly ten times than Lee ( $7 \times 7$ ).

TABLE VI  
COMPUTATIONAL TIMES (IN MINUTES) OF LEE, WAVELET,  
AND SDC FOR THE SAR IMAGE IN FIG. 12

	Lee	Wavelet	SDC
Selangor	195.90	22.28	19.94

## V. CONCLUSION

A subspace-based denoising technique for SAR images has been presented and tested. The proposed technique (SDC) is based on linear estimator and reduced-rank subspace model to estimate the clean image from the corrupted one with speckle noise. The validity of the reduced-rank model in representing different SAR images has been verified and used to enhance the performance of the linear estimator. The capability of the proposed SDC technique in efficiently representing SAR images with reduced-rank values has been discussed and verified.

Next, the performance of the SDC has been tested with simulated three-look amplitude data and compared with Lee and wavelet. The results indicate less noise variance reduction capability by SDC than Lee and wavelet but with less blur, less artifacts, and better preservation of the radiometric edges of the targets.

With the real scenario, the SDC, Lee, and wavelet are run with the intensity format three-look SAR image for Selangor area in Malaysia. Two stationary areas are selected, and the performances are calculated in terms of noise reduction and preservation of the autocorrelation profiles. The results show moderate noise reduction by the proposed SDC filter in comparison to Lee but with significantly less blurring effect and a comparable performance to wavelet but with less artifacts. The autocorrelation results show better preservation of autocorrelation and textures of the image by SDC than Lee and wavelet. Moreover, the capability of the algorithms in preserving and cleaning the radiometric edges is tested through the intensity profiles of transects pass through point and hard target. The results show better performance by SDC and wavelet in comparison to Lee. Finally, the computational complexity of the algorithms is compared, and the results show approximately ten times less needed computational time by SDC and wavelet than Lee.

## ACKNOWLEDGMENT

The authors would like to thank the Malaysian Remote Sensing Agency for providing the validation data and the anonymous reviewers for their effort and constructive comments which helped in properly addressing the different issues and resulted in stronger proof of the proposed approach.

## REFERENCES

- [1] S. Kuttikkad and R. Chellappa, "Statistical modeling and analysis of high-resolution synthetic aperture radar images," *Statist. Comput.*, vol. 10, no. 2, pp. 133–145, Apr. 2000.
- [2] J. W. Goodman, "Some fundamental properties of speckle," *J. Opt. Soc. Amer.*, vol. 66, no. 11, pp. 1145–1150, Nov. 1976.
- [3] B. Tso and P. Mather, *Classification Methods for Remotely Sensed Data*, 2nd ed. Boca Raton, FL, USA: CRC Press, 2009.
- [4] J. S. Lee, "Digital image enhancement and noise filtering by use of local statistics," *IEEE Trans. Pattern Anal. Mach. Intell.*, vol. PAMI-2, no. 2, pp. 165–168, Mar. 1980.



- [5] V. S. Frost, J. A. Stiles, K. S. Shanmugan, and J. C. Holtzman, "A model for radar images and its application to adaptive digital filtering of multiplicative noise," *IEEE Trans. Pattern Anal. Mach. Intell.*, vol. PAMI-4, no. 2, pp. 157–166, Mar. 1982.
- [6] D. Kuan, A. Sawchuk, T. Strand, and P. Chavel, "Adaptive restoration of images with speckle," *IEEE Trans. Acoust., Speech, Signal Process.*, vol. 35, no. 3, pp. 373–383, Mar. 1987.
- [7] A. Lopes, R. Touzi, and E. Nezry, "Adaptive speckle filters and scene heterogeneity," *IEEE Trans. Geosci. Remote Sens.*, vol. 28, no. 6, pp. 992–1000, Nov. 1990.
- [8] J. S. Lee, "Speckle suppression and analysis for synthetic aperture radar images," *Opt. Eng.*, vol. 25, pp. 636–643, May 1986.
- [9] F. T. Ulaby, F. Kouyate, B. Brisco, and T. H. L. Williams, "Textural information in SAR images," *IEEE Trans. Geosci. Remote Sens.*, vol. GE-24, no. 2, pp. 235–245, Mar. 1986.
- [10] L. Jong-Sen, W. Jen-Hung, T. L. Ainsworth, C. Kun-Shan, and A. J. Chen, "Improved sigma filter for speckle filtering of SAR imagery," *IEEE Trans. Geosci. Remote Sens.*, vol. 47, no. 1, pp. 202–213, Jan. 2009.
- [11] H. Guo, J. E. Odegaard, M. Lang, R. A. Gopinath, I. W. Selesnick, and C. S. Burrus, "Wavelet based speckle reduction with application to SAR based ATDR," in *Proc. IEEE ICIP*, 1994, vol. 1, pp. 75–79.
- [12] M. Vetterli and J. Kovacevic, *Wavelets and Subband Coding*. Upper Saddle River, NJ, USA: Prentice-Hall, 1995.
- [13] S. Solbo and T. Eltoft, "Homomorphic wavelet-based statistical despeckling of SAR images," *IEEE Trans. Geosci. Remote Sens.*, vol. 42, no. 4, pp. 711–721, Apr. 2004.
- [14] J. R. Sveinsson and J. A. Benediktsson, "Speckle reduction and enhancement of SAR images using multiwavelets and adaptive thresholding," in *Proc. SPIE Conf. Image Signal Process. Remote Sens. V*, vol. 3871, *EUROPTO Series*, S. B. Serpico, Ed., 1999, pp. 239–250.
- [15] S. Fukuda and H. Hirokawa, "Smoothing effect of wavelet-based speckle filtering: The Haar basis case," *IEEE Trans. Geosci. Remote Sens.*, vol. 37, no. 2, pp. 1168–1172, Mar. 1999.
- [16] X. Hua, L. E. Pierce, and F. T. Ulaby, "Statistical properties of logarithmically transformed speckle," *IEEE Trans. Geosci. Remote Sens.*, vol. 40, no. 3, pp. 721–727, Mar. 2002.
- [17] F. Argenti and L. Alparone, "Speckle removal from SAR images in the undecimated wavelet domain," *IEEE Trans. Geosci. Remote Sens.*, vol. 40, no. 11, pp. 2363–2374, Nov. 2002.
- [18] J. J. Ranjani and S. J. Thiruvengadam, "Dual-tree complex wavelet transform based SAR despeckling using interscale dependence," *IEEE Trans. Geosci. Remote Sens.*, vol. 48, no. 6, pp. 2723–2731, Jun. 2010.
- [19] Y. Ephraim and H. L. V. Trees, "A signal subspace approach for speech enhancement," *IEEE Trans. Speech Audio Process.*, vol. 3, no. 4, pp. 251–266, Jul. 1995.
- [20] L. Sendur and I. W. Selesnick, "Bivariate shrinkage functions for wavelet-based denoising exploiting interscale dependency," *IEEE Trans. Signal Process.*, vol. 50, no. 11, pp. 2744–2756, Nov. 2002.
- [21] L. Sendur and I. W. Selesnick, "Bivariate shrinkage with local variance estimation," *IEEE Signal Process. Lett.*, vol. 9, no. 12, pp. 438–441, Dec. 2002.
- [22] J. W. Goodman, *Statistical Properties of Laser Speckle Patterns*. Heidelberg, Germany: Springer-Verlag, 1980.
- [23] F. T. Ulaby, *Handbook of Radar Scattering Statistics for Terrain*. Norwood, MA, USA: Artech House, 1989.
- [24] D. H. Hoekman, "Speckle ensemble statistics of logarithmically scaled data," *IEEE Trans. Geosci. Remote Sens.*, vol. 29, no. 1, pp. 180–182, Jan. 1991.
- [25] J.-S. Lee and E. Pottier, *Polarimetric Radar Imaging: From Basics to Applications*. Boca Raton, FL, USA: CRC Press, 2009.
- [26] P. S. K. Hansen, "Signal Subspace Methods for Speech Enhancement," Ph.D. dissertation, Tech. Univ. Denmark, Lyngby, Denmark, 1997.
- [27] A. Rezayee and S. Gazor, "An adaptive KLT approach for speech enhancement," *IEEE Trans. Speech Audio Process.*, vol. 9, no. 2, pp. 87–95, Feb. 2001.
- [28] D. Luenberger, *Linear and Nonlinear Programming*, 2nd ed. Reading, MA, USA: Addison-Wesley, 1984.
- [29] S. Haykin, *Adaptive Filter Theory*. Englewood Cliffs, NJ, USA: Prentice-Hall, 1991.
- [30] B. D. Moor, J. Staar, and J. Vandewalle, "Oriented energy and oriented signal-to-signal ratio concepts in the analysis of vector sequences and time series," in *SVD and Signal Processing*. Amsterdam, The Netherlands: North Holland, 1988, pp. 209–232.
- [31] G. Golub and C. V. Loan, *Matrix Computations*, 3rd ed. Baltimore, MD, USA: Johns Hopkins Univ. Press, 1996.
- [32] B. D. Moor, "The singular value decomposition and long and short spaces of noisy matrices," *IEEE Trans. Signal Process.*, vol. 41, no. 9, pp. 2826–2838, Sep. 1993.
- [33] S. Deerwester, S. T. Dumais, G. W. Furnas, T. K. Landauer, and R. Harshman, "Indexing by latent semantic analysis," *J. Amer. Soc. Inform. Sci.*, vol. 41, no. 6, pp. 391–407, Sep. 1990.
- [34] M. W. Berry, S. T. Dumais, and G. W. O'Brien, "Using linear algebra for intelligent information retrieval," *SIAM Rev.*, vol. 37, no. 4, pp. 573–595, Dec. 1995.
- [35] K. Konstantinides and K. Yao, "Statistical analysis of effective singular values in matrix rank determination," *IEEE Trans. Acoust., Speech, Signal Process.*, vol. 36, no. 5, pp. 757–763, May 1988.
- [36] M. Petrou and P. Sevilla, *Image Processing: Dealing with Texture*, 1st ed. Hoboken, NJ, USA: Wiley, 2006.
- [37] D. Donoho, "De-noising by soft-thresholding," *IEEE Trans. Inform. Theory*, vol. 41, no. 3, pp. 613–627, May 1995.



**Norashikin Yahya** (M'05) received the B.Eng. degree (Hons) in electronic engineering specializing in communications from the University of Sheffield, Sheffield, U.K., in 2001 and the M.Sc. degree in electrical engineering from Lehigh University, Bethlehem, PA, USA, in 2004. She is currently working toward the Ph.D. degree at the Universiti Teknologi PETRONAS, Tronoh, Malaysia, where her Ph.D. dissertation is on noise reduction using signal subspace techniques.

She is currently a Lecturer with the Universiti Teknologi PETRONAS. Her research interests are in the area of signal and image processing and its applications.



**Nidal S. Kamel** (SM'04) received the Ph.D. degree (Hons) from the Technical University of Gdańsk, Gdańsk, Poland, in 1993.

His Ph.D. work focused on subspace-based array signal processing for direction-of-arrival estimation. He is currently an Associate Professor with the Universiti Teknologi PETRONAS, Tronoh, Malaysia. Since 1993, he has been involved in research projects related to estimation theory, noise reduction, optimal filtering, and pattern recognition. He developed a single-trial subspace-based technique for the extraction of the event-related potentials from brain background noise and introduced a subspace-based data glove system for online signature verification. His present research interest is in the implementation of subspace techniques in synthetic aperture radar and ultrasound image enhancement as well as in various areas in brain signal processing.



**Aamir Saeed Malik** (SM'10) received the B.S. degree in electrical engineering from the University of Engineering and Technology, Lahore, Pakistan, the M.Sc. degree in nuclear engineering from Quaid-i-Azam University, Islamabad, Pakistan, and the M.Sc. degree in information and communication and the Ph.D. degree in information and mechatronics from Gwangju Institute of Science and Technology, Gwangju, Korea.

He has more than 15 years of research experience and has worked for IBM, Hamdard University, Karachi, Pakistan, Government of Pakistan, Yeungnam University, Gyeongsan, Korea, and Hanyang University, Seoul, Korea, during his career. He is currently an Associate Professor with the Universiti Teknologi PETRONAS, Tronoh, Malaysia. His research interests include biomedical signal and image processing, visual surveillance, remote sensing, and brain sciences.